

Unfolding the X-ray Spectral Curvature of Mkn 421 for Further Clues

Pranjupriya Goswami^{1*}, Sunder Sahayanathan^{2,3 †}, Atreyee Sinha⁴ & Rupjyoti Gogoi¹

¹*Department of Physics, Tezpur University, Napaam - 784028, India*

²*Astrophysical Sciences Division, Bhabha Atomic Research Centre, Mumbai - 400085, India*

³*Homi Bhabha National Institute, Mumbai - 400094, India*

⁴*Laboratoire Univers et Particules de Montpellier, Université de Montpellier, CNRS, Montpellier - 34095, France.*

Accepted XXX. Received YYY; in original form ZZZ

ABSTRACT

The X-ray observations of Mkn 421 show significant spectral curvature that can be reproduced by a log-parabola function. The spectra can also be fitted by an analytical model considering synchrotron emission from an electron distribution that is accelerated at a shock front with an energy-dependent diffusion (EDD model). The spectral fit of *NuSTAR* and *Swift*-XRT observations using EDD model during different flux states reveal the model parameters are strongly correlated. We perform a detailed investigation of this correlation to decipher the information hidden underneath. The model predicts the synchrotron peak energy to be correlated with the peak spectral curvature which is consistent with the case of Mkn 421. Expressing the energy dependence of the diffusion in terms of the magnetohydrodynamic turbulence energy index, it appears the turbulence shifts from Kolmogorov/Kraichnan type to Bohm limit during high flux states. Further, the correlation between the best-fit parameters of EDD model lets us derive an expression for the product of source magnetic field (B) and jet Doppler factor (δ) in terms of synchrotron and Compton peak energies. The synchrotron peak energy is obtained using the simultaneous *Swift*-XRT–*NuSTAR* observations; whereas, the Compton peak energy is estimated by performing a linear regression analysis of the archival spectral peaks. The deduced δB varies over a wide range; however, it satisfies reasonably well with the values estimated solely from the spectral peak energies independent of the EDD model. This highlights the plausible connection between the microscopic description of the electron diffusion with the macroscopic quantities deciding the broadband spectrum of Mkn 421.

Key words: galaxies: active – BL Lacertae objects: individual: Mkn 421 – acceleration of particles – diffusion – X-rays: galaxies

1 INTRODUCTION

Mkn 421 is one of the nearest BL Lac type of active galactic nuclei located at redshift $z = 0.031$ (Punch et al. 1992). The spectra of these class of sources extend from radio to GeV/TeV energies and also found to be rapidly varying in a time-scale of days to few minutes (McEney et al. 1997; Tanihata et al. 2004; Tramacere et al. 2009; Donnarumma et al. 2009;

Aleksić et al. 2015a; Hovatta et al. 2015; Sinha et al. 2015). The detection of very high energy radiation and the rapid variability confirm the emission is significantly Doppler boosted due to the relativistic motion of the emitting region (Dondi & Ghisellini 1995). Their spectral energy distribution (SED) is characterized by two prominent peaks with the low energy component peaking at UV/X-ray energy and well understood to be synchrotron emission from a non-thermal electron distribution (Padovani & Giommi 1995). The high energy component peaking at γ -ray energy is usually attributed to synchrotron self Compton emission (Abdo et al. 2011; Acciari et al. 2011). In

* E-mail: pranjupriya.g@gmail.com

† Email: sunder@barc.gov.in

case of Mkn421, this interpretation of high energy emission process is further supported by the correlated X-ray/TeV flares and the quadratic dependence of the X-ray and γ -ray fractional variability (Mastichiadis & Kirk 1997; Błażejowski et al. 2005; Giebels et al. 2007; Fossati et al. 2008; Katarzyński & Walczewska 2010; Bartoli et al. 2011; Kapanadze et al. 2018a,b). Interestingly, its synchrotron peak is observed to vary over a broad energy range during different flux states (Aleksić et al. 2015b; Kapanadze et al. 2016; Bartoli et al. 2016; Baloković et al. 2016).

The narrow band X-ray spectra of Mkn421 exhibits significant curvature that cannot be interpreted by a simple power-law or a power-law with an exponential cutoff (Fossati et al. 2000; Krawczynski et al. 2001; Massaro et al. 2004; Tramacere et al. 2007; Yan et al. 2013). The curvature extends even at hard X-rays and hence cannot be easily attributed to the one arising from the spectral changeover at the peak of the synchrotron component (Fossati et al. 2008; Horan et al. 2009). On the other hand, a log-parabola function is able to explain the X-ray spectral curvature of Mkn421 over a narrow band; however, it fails to reproduce the optical/UV flux when extended to low energies (Massaro et al. 2004; Sinha et al. 2015).

A log-parabola spectrum demands the underlying electron distribution also to be a log-parabola and such an electron distribution can be attained when the particle acceleration probability is energy-dependent (Massaro et al. 2004). The probability for confining the particle within the acceleration region will decrease with the increase in the gyroradius and hence, the acceleration probability can be energy-dependent. This model predicts the synchrotron peak energy to be anti-correlated with its curvature (Tramacere et al. 2007). Further using Monte Carlo simulations, Tramacere et al. (2011) showed the electron distribution resulting from a stochastic acceleration can be approximated by a log-parabola function. Using this time-dependent model, the authors studied the evolution of the accelerated electron distribution under different types of turbulent energy spectrum. They showed the curvature at the peak energy of the accelerated electron distribution is related to the acceleration time-scale associated with the momentum diffusion. Subsequently, they predicted the peak spectral curvature of the synchrotron spectrum to be anti-correlated with the peak energy. Analysis of the log-parabola X-ray spectral shape of Mkn421 and BL Lacs in general, are largely inconclusive. Modelling the X-ray observation of Mkn421 and other TeV BL Lacs, during 1997-2006, using a log-parabola model have revealed an anti-correlation between the peak spectral curvature and the peak energy consistent with the stochastic acceleration process (Tramacere et al. 2007; Massaro et al. 2008; Tramacere et al. 2009, 2011). On the contrary, X-ray analysis for Mkn421 using *Swift*-XRT/*NuSTAR* data during 2005-2008 and during 2009-2013 (Sinha et al. 2015; Kapanadze et al. 2016, 2018a,b) have shown weak negative/no correlation between these quantities.

Time-dependent models, tracing the evolution of the accelerated particle distribution and the emission spectra, under energy-dependent acceleration and/or escape time-scales have been studied by several authors, and are capable of producing variety of spectra (Stawarz & Petrosian 2008; Lewis et al. 2016; Zheng et al. 2014; Summerlin & Baring

2011; Baring et al. 2017; Kakuwa 2016; Asano et al. 2014; Becker et al. 2006; Katarzyński et al. 2006). For stochastic acceleration process, the energy-dependence of the acceleration and escape time-scale can be expressed as $t_{\text{acc}} \sim E^{2-q}$ and $t_{\text{esc}} \sim E^{q-2}$ where, E is the particle energy and q is the power-law index of the magnetohydrodynamic turbulent spectrum (Stawarz & Petrosian 2008; Tramacere et al. 2011). Additionally, in case of shock acceleration, t_{acc} is also determined by the time-scale at which particles cycle across the shock (Lewis et al. 2016). The value of q can range from $q = 1$ associated with Bohm diffusion, to $q = 2$ under hard-sphere approximation (Kirk et al. 1998; Asano et al. 2014). In case of Kolmogorov type turbulence $q = 5/3$ and for Kraichnan type turbulence $q = 3/2$ (Teraki & Asano 2019). Often these time-dependent models involve large number of parameters and are mainly used to understand the observations from a theoretical perspective. Instead, reducing the accelerated particle distribution and the emission spectrum into a simple mathematical form (similar to a log-parabola function) can help us to perform a detailed statistical analysis of the observed data that provide a deeper insight into the physics of the source (e.g. Massaro et al. 2004; Tramacere et al. 2011; Goswami et al. 2018; Jagan et al. 2018).

Under the simplistic approach, a curved spectrum can also be interpreted as an outcome of the energy-dependent diffusion from the acceleration region (EDD model). The synchrotron spectral shape due to this model is determined by two parameters and hence a direct comparison with the log-parabola function is possible. In our earlier work, we demonstrate the capability of this model to fit the *NuSTAR* and *Swift*-XRT X-ray observations of Mkn421 and the spectral fits are comparable with that of a log-parabola (Goswami et al. 2018, hereafter Paper-I). Unlike the later, the best-fit parameters are well correlated in the case of EDD model and the correlation is much stronger when the fitting is performed on the *NuSTAR* data alone.

In this work, we revisit the EDD model to investigate the correlation between the fit parameters and interpret the physical conditions of Mkn421 during various flux states. The model is also upgraded by considering the finite width of the synchrotron single particle emissivity rather than a δ -function approximation and the total emissivity is estimated numerically. Further, we study the salient features of the observed spectrum that can be verified through observations. The modified EDD model is applied to *NuSTAR* and *Swift*-XRT X-ray observations of Mkn421 and the best-fit parameters are obtained. In addition, we also update our study by including the recent X-ray observations. The energy-dependence of the diffusive process can represent the magnetohydrodynamic turbulence in blazar jet and hence, the EDD model can provide a convenient way to probe the same. Finally, we show that the correlation between the best-fit EDD parameters can be used to establish a relation between the energy dependence of the electron escape time-scale, and the product of the source magnetic field and the jet Doppler factor. This illustrates that the information regarding the physical parameters deciding the broadband emission of the source is concealed within the X-ray spectral shape. In the following section, we describe the formalism of EDD model in detail and observational features of the syn-

chrotron spectrum. In §3, we describe the analysis of the X-ray spectra of Mkn 421 and present the correlation study results. Following this in §4, we show how the correlation between the best-fit parameters can be used to obtain a relation between the energy dependence of the diffusive process and the source parameters, and extend this for the case of Mkn 421.

2 ENERGY-DEPENDENT DIFFUSION (EDD) MODEL

We consider the non-thermal electron distribution $N_a(E)$, responsible for the broadband emission in blazars, to be accelerated at a shock front through first-order Fermi mechanism and its evolution is governed by (Kardashev 1962; Kirk et al. 1998; Kusunose et al. 2000)

$$\frac{\partial N_a(E)}{\partial t} + \frac{\partial}{\partial E} \left[\left(\frac{E}{t_{\text{acc}}} - \beta_s E^2 \right) N_a(E, t) \right] = Q_0 \delta(E - E_{\text{inj}}) - \frac{N_a(E, t)}{t_{\text{esc}}} \quad (1)$$

Here, E is the electron energy and the particle acceleration rate at the shock front is parameterized as $1/t_{\text{acc}}$ while the radiative loss rate due to synchrotron emission is given as $\beta_s E^2$. β_s is related to the magnetic energy density of the region in vicinity to the shock front (Kirk et al. 1998; Rybicki & Lightman 1985). We consider the case, where the electrons gain energy mainly by crossing the shock front and the change in energy by individual scatterings at magnetic inhomogeneities are neglected. Under this scenario, t_{acc} will be determined by the time-scale at which particles cycle across the shock, and if we assume the spatial diffusion coefficient in the vicinity of the shock to be constant then, $t_{\text{acc}} = \text{constant}$ (Lewis et al. 2016). Further, we assume a monoenergetic injection of electron at energy E_{inj} and the accelerated electron escape from the acceleration region (vicinity of the shock front) at a rate $1/t_{\text{esc}}$. The magnetohydrodynamic turbulence in jet flow can cause the spatial diffusion of the electron to be energy-dependent and we imitate this by considering the electron escape time-scale from acceleration region to be of the form,

$$t_{\text{esc}}(E) \propto \left(\frac{E}{E_0} \right)^{-\kappa} \quad (2)$$

where, κ determines the energy dependence of the electron escape and the proportionality constant is the electron escape time-scale corresponding to electron energy E_0 . Expressing the radiative loss in terms of maximum accelerated electron energy $E_{\text{max}} = (\beta_s t_{\text{acc}})^{-1}$ (Kirk et al. 1998), the steady state condition of equation (1) will be

$$\frac{d}{dE} \left[\left(1 - \frac{E}{E_{\text{max}}} \right) \frac{E}{t_{\text{acc}}} N_a(E) \right] = Q_0 \delta(E - E_{\text{inj}}) - \frac{N_a(E)}{t_{\text{esc}}} \quad (3)$$

Under constant t_{acc} and for $E_{\text{inj}} < E \ll E_{\text{max}}$, equation (3) can be reduced to (Jagan et al. 2018, Paper-I).

$$\frac{d \ln[EN_a(E)]}{d \ln E} \approx -\frac{t_{\text{acc}}}{t_{\text{esc}}} \quad (4)$$

Using equation (2), the solution of above will be

$$N_a(E) \propto E^{-1} \exp \left[-\frac{\xi_0}{\kappa} \left(\frac{E}{E_0} \right)^\kappa \right] \quad (5)$$

Here, ξ_0 is the ratio $t_{\text{acc}}/t_{\text{esc}}$ at energy E_0 . The accelerated electrons will eventually escape from the acceleration region and lose their energy through synchrotron and inverse Compton emission processes. Then the steady state equation governing the electron distribution N_c responsible for the observed emission spectrum will be (Kardashev 1962; Kirk et al. 1998; Kusunose et al. 2000),

$$-\frac{d}{dE} \left[BE^2 N_c(E) \right] = \frac{N_a(E)}{t_{\text{esc}}} \quad (6)$$

where, BE^2 is the radiative energy loss rate and the right-hand side is the injection from the acceleration region. Using equations (2) and (5) we get,

$$N_c(E) \propto E^{-2} \exp \left[-\frac{\xi_0}{\kappa} \left(\frac{E}{E_0} \right)^\kappa \right] \quad (7)$$

The observed synchrotron flux F_ϵ at energy ϵ can be attained by convolving $N_c(E)$ with the single particle emissivity function after accounting for the effects due to relativistic motion of the emission region and cosmology (Begelman et al. 1984; Rybicki & Lightman 1985):

$$F_\epsilon \propto \int_0^\infty f \left(\frac{1+z}{\delta} \frac{\epsilon}{\epsilon_c} \right) N_c(E) dE; \quad (8)$$

$$\epsilon_c = \frac{3heB}{16m^2c^3} \left(\frac{E^2}{mc^2} \right) \quad (9)$$

Here, z is the redshift of the source, δ is the relativistic Doppler factor of the emission region, h is the Planck constant, e and m are the charge and mass of the electron, c is the velocity of light and B is the source magnetic field responsible for the synchrotron emission. The synchrotron power function $f(x)$ is given by

$$f(x) = x \int_x^\infty K_{5/3}(\zeta) d\zeta \quad (10)$$

where, $K_{5/3}$ is the modified Bessel function of order $5/3$. Introducing

$$\alpha = \left(\frac{1+z}{\delta} \right) \frac{16m^2c^3}{3heB} \quad (11)$$

From equation (8) we obtain,

$$F_\epsilon \propto \frac{1}{\sqrt{\epsilon}} \int_0^\infty f(x) \exp \left[-\frac{\psi}{\kappa} \left(\frac{\epsilon}{mc^2 x} \right)^{\kappa/2} \right] \frac{dx}{\sqrt{x}} \quad (12)$$

where,

$$\psi = \xi_0 \left(\frac{\alpha m^2 c^4}{E_0^2} \right)^{\kappa/2} \quad (13)$$

Equation (12) describes the observed synchrotron spectrum in terms of two parameters, ψ and κ . It will be evident from the next section that the parameter κ governs the spectral curvature and ψ determines the spectral index at a given energy.

2.1 Synchrotron Spectral Slope

The synchrotron spectrum described by equation (12) deviates significantly from a power-law and hence the spectral slope will be a function of the photon energy ϵ . From equation (4), the slope of the accelerated particle distribution in logarithmic scale will be

$$\frac{d \ln N_a(E)}{d \ln E} = - \left(1 + \frac{t_{\text{acc}}}{t_{\text{esc}}} \right) \quad (14)$$

Since, $N_c(E) \propto N_a(E)/E$ the slope of the electron distribution responsible for the radiation in logarithmic scale will be

$$\frac{d \ln N_c}{d \ln E} = - \left(2 + \frac{t_{\text{acc}}}{t_{\text{esc}}} \right) \quad (15)$$

Considering a δ -function approximation for the single particle emissivity, the synchrotron emissivity due to the electron distribution N_c will be (Finke et al. 2008; Böttcher & Dermer 2010; Sahayanathan & Godambe 2012)

$$j_{\text{syn}}(\epsilon) \propto \epsilon^{1/2} N_c \left(\sqrt{\frac{\epsilon}{\epsilon_L}} \right) \quad (16)$$

the synchrotron spectral slope at the photon energy ϵ will then be,

$$\frac{d \ln j_{\text{syn}}}{d \ln \epsilon} \approx -\frac{1}{2} \left[1 + \xi_0 \left(\frac{E}{E_0} \right)^\kappa \right] \quad (17)$$

Where, E is the energy of electron responsible for the emission at photon energy ϵ . Since $\epsilon \propto E^2$, the spectral slope in ϵj_{syn} will be,

$$\frac{d \ln(\epsilon j_{\text{syn}})}{d \ln \epsilon} \approx \frac{1}{2} \left[1 - \xi_0 \left(\frac{\epsilon}{\epsilon_0} \right)^{\kappa/2} \right] \quad (18)$$

Here, ϵ_0 is the energy of the photon emitted by the electron of energy E_0 . If we approximate the function $f(x)$ in equation (12) by a δ -function peaking at ≈ 0.29 (Rybicki & Lightman 1985), the synchrotron spectral slope in terms of the parameters ψ and κ can be obtained as

$$\frac{d \ln(\epsilon F_\epsilon)}{d \ln \epsilon} \approx \frac{1}{2} \left[1 - \psi \left(\frac{\epsilon}{0.29 mc^2} \right)^{\kappa/2} \right] \quad (19)$$

2.2 Synchrotron spectral peak and curvature

At the photon energy ϵ_p , where the flux peaks in ϵF_ϵ representation, the spectral slope will be zero. Hence, from equation (18) we obtain,

$$\epsilon_p = \epsilon_0 \xi_0^{-2/\kappa} \quad (20)$$

The spectral curvature at the photon energy ϵ_p will be¹

$$\begin{aligned} H_p &= \left. \frac{d^2 \ln \epsilon j_{\text{syn}}}{d \ln \epsilon^2} \right|_{\epsilon=\epsilon_p} \\ &= -\frac{\kappa}{4} \end{aligned} \quad (21)$$

¹ The curvature of a function $y = g(x)$ is defined as $H = g''/(1 + g'^2)^{1.5}$

The above relation illustrates the spectral curvature where the synchrotron spectrum peaks, is governed by the parameter (κ) which determines the energy dependence of the escape time-scale. Since the synchrotron flux is maximum at ϵ_p , $\kappa > 0$. Using equation (20), H_p can be written in terms of ϵ_p as

$$H_p = \frac{1}{2} \frac{\ln \xi_0}{\ln(\epsilon_p/\epsilon_0)} \quad (22)$$

Alternatively, using equation (19), H_p can also be expressed in terms of ψ and ϵ_p as

$$H_p \approx \frac{1}{2} \frac{\ln \psi}{\ln \left(\frac{\epsilon_p}{0.29 mc^2} \right)} \quad (23)$$

Since $H_p < 0$, we attain the condition that $\epsilon_p < 0.29 mc^2$ for $\psi > 1$ and $\epsilon_p > 0.29 mc^2$ for $\psi < 1$. In the former case, the curvature increases with the peak energy and it is reverse in case of the latter. In other words, a positive correlation between κ and $\ln \epsilon_p$ demands $\psi > 1$ and vice-versa. Similar conclusion can also be obtained from equation (20) since $\kappa > 0$.

3 SPECTRAL ANALYSIS

The X-ray spectrum of the BL Lac object Mkn 421 is analysed using the EDD model discussed in the previous section. To obtain the synchrotron flux, the double integration given by equations (10) and (12) needs to be evaluated numerically. However, to improve the computational speed we approximate $f(x)$ as (Melrose, D.B. 1980)

$$f(x) = 1.8 x^{0.3} \exp(-x) \quad (24)$$

and this reduces the equation (12) to single integration which is evaluated using 80 point Gaussian-quadratures (Press et al. 1992). The spectral shape of the EDD model is described by two parameters, namely ψ and κ . Alternatively, one can choose the fit parameters to be ϵ_p and κ using equation (19). Since the curvature at ϵ_p is $-\kappa/4$, the latter approach provides a direct analysis of the synchrotron spectral peak and the associated curvature. However, this demands the observation to be available in the neighbourhood of ϵ_p for convincing results. We developed two separate numerical codes corresponding to these choices of fit parameters and added them as local models in XSPEC (Arnaud 1996). Using these models, the X-ray observations of Mkn 421 are fitted adopting a χ^2 -minimization technique.

In the present work, we repeated the analysis of 20 NuSTAR pointings of the source Mkn 421 presented in our earlier work (Paper-I) using the above two models. In addition, we update our analysis by including 4 new observations by NuSTAR during 2017 and the details are given in Table 1. The details about the data reduction procedure are described in Paper-I. The spectral fit results are summarized in Table 2. Equation (13) implies a linear correlation between $\ln \psi$ and κ , provided α/E_0^2 is constant. In Figure 1 (bottom panel), we show the scatter plot between $\ln \psi$ and κ and the Pearson correlation study resulted in a positive correlation with the correlation coefficient $r = 0.95$ and null-hypothesis probability $P_p = 1.74 \times 10^{-12}$. The Spearman rank correlation study results are, the correlation coefficient $\rho = 0.92$ and

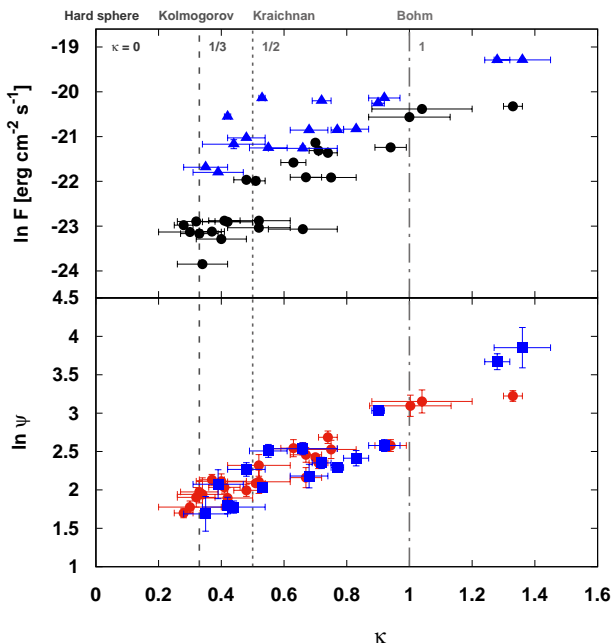


Figure 1. The correlation plots between the best-fit EDD model parameters and the integrated flux of Mkn 421 using *Swift*-XRT and *NuSTAR* observations. **Top panel:** Scatter plots between 3–10 keV integrated flux v/s κ using *NuSTAR* data alone is represented by black circles and 0.3–10 keV integrated flux v/s κ for simultaneous XRT – *NuSTAR* data is shown by blue triangles. **Bottom panel:** Scatter plot between $\ln \psi$ v/s κ . The red circles indicate the correlation using *NuSTAR* data alone, whereas the blue squares indicate the same for the simultaneous XRT – *NuSTAR* data. The vertical lines at $\kappa = 0, 1/3, 1/2$ and 1 represent the various type of turbulences corresponding to hard-sphere, Kolmogorov, Kraichnan and Bohm as discussed in §3.1.

the null-hypothesis probability $P_s = 1.02 \times 10^{-10}$. Presence of this strong correlation, besides favouring the EDD model, it indicates the quantity δBE_0^2 is nearly constant for Mkn 421 independent of the observed flux states. We will discuss more about this constancy in §4.

The spectral fit of *NuSTAR* observations of Mkn 421 using EDD model satisfies the condition $\psi > 1$ for all flux states. Hence, from equations (23) and (20), a linear correlation is expected between κ and $\ln \epsilon_p$. To perform the spectral fitting with κ and ϵ_p as free parameters, *NuSTAR* observations alone would not be sufficient since the synchrotron spectral peak lies at energies much lower than its operational energy range. Therefore, we selected the *NuSTAR* observations for which simultaneous observations by *Swift*-XRT at soft X-ray energies are available. In addition to the 10 observations presented in Paper-I, we updated our analysis by including 6 simultaneous observations with 2 during 2013 and 4 during 2017 while maintaining the observation time gap between the X-ray instruments within ~ 3 hrs. The observational details are given in Table 1 and the XRT data reduction procedures are described in Paper-I. The results of the spectral fit using EDD model with κ and ϵ_p as fit parameters are given in Table 3 and the scatter plot between $\ln \epsilon_p$ and κ is shown in Figure 2 (blue circles). A strong positive

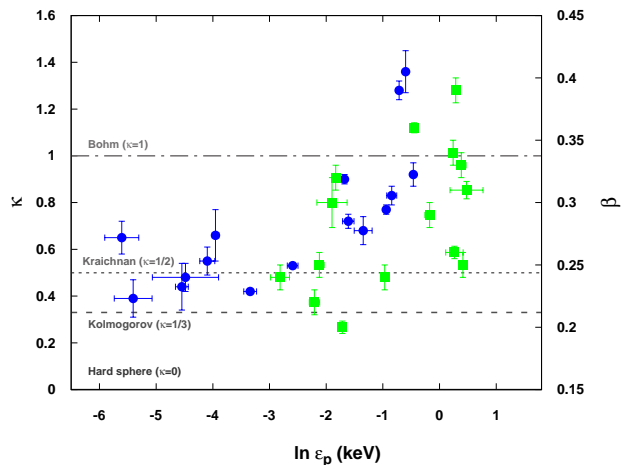


Figure 2. The scatter plots showing correlation between the curvature parameter and the synchrotron peak using EDD and *eplogpar* model fit for 16 different simultaneous XRT – *NuSTAR* observations. The blue circles represent plot between the parameters κ and ϵ_p obtained from the EDD model fit, whereas, the green boxes represent the plot between β and ϵ_p obtained from *eplogpar*. The horizontal lines at $\kappa = 0, 1/3, 1/2$ and 1 represent the various type of turbulences as discussed in §3.1.

correlation is observed between $\ln \epsilon_p$ and κ with $r = 0.86$; $P_p = 2.42 \times 10^{-5}$ and $\rho = 0.91$; $P_s = 7.01 \times 10^{-7}$, and this is again consistent with the EDD model. For comparison, we fitted the simultaneous XRT – *NuSTAR* observations using *eplogpar* model inbuilt in XSPEC (Tramacere et al. 2007, 2009). The fit results are given in Table 3 and the scatter plot between the synchrotron peak ϵ_p and the curvature parameter β of *eplogpar* is shown in Figure 2 (green points). We see a trend of β increasing with ϵ_p , with marginal correlation coefficients of $r = 0.56$ ($P_p = 0.02$) and $\rho = 0.53$ ($P_s = 0.03$). For the correlation study, we have used only those data points with associated uncertainty less than 20%. This is to assure that results are not biased by the large uncertainties.

We also fitted the simultaneous XRT – *NuSTAR* observations using the EDD model with ψ and κ as fit parameters and this reduced the correlation with $r = 0.90$; $P_p = 1.65 \times 10^{-6}$ and $\rho = 0.86$; $P_s = 5.14 \times 10^{-6}$. In Figure 1, the scatter plot between the best-fit $\ln \psi$ and κ is shown as blue squares for the simultaneous XRT – *NuSTAR* observations. The reduction in the correlation between $\ln \psi$ and κ with the inclusion of soft X-ray data implies the EDD model may not be favourable at low energies. A careful observation of equations (2) and (3) may highlight the plausible reason for this. As the particle escape rate is an increasing function of particle energy ($\because \kappa > 0$), the effect of the EDD model will be more prominent at higher particle energy rather than the lower ones. This is also consistent with the case that the probability to confine electron within the acceleration region decreases with the increase in energy. Accordingly, the hard X-ray spectra will reflect the EDD model better than the soft X-ray.

Table 1. Summary of the additional 6 pointings of simultaneous XRT – *NuSTAR* observations of Mkn 421.

<i>Swift</i> -XRT			<i>NuSTAR</i>		
Obs. ID	Obs. date & time (dd-mm-yy)	Exposure (sec)	Obs. ID	Obs. date & time (dd-mm-yy)	Exposure (sec)
00032792001	2013-04-11 T03:41:30	3489	60002023025	2013-04-11 T01:01:07	57509
00032792002	2013-04-14 T00:38:59	6327	60002023029	2013-04-13 T21:36:07	16510
00034228166	2017-03-27 T22:12:57	1119	60202048008	2017-03-27 T21:51:09	31228
00034228146	2017-03-01 T00:26:19	85	60202048006	2017-02-28 T22:11:09	23906
00034228110	2017-01-04 T00:06:57	6021	60202048002	2017-01-03 T23:51:09	23691
00081926001	2017-01-31 T23:27:57	1009	60202048004	2017-01-31 T23:46:09	21564

Table 2. The best-fit EDD model parameters for 24 pointings of *NuSTAR* observations.

<i>NuSTAR</i> Obs. ID	ψ	κ	ϵ_p	χ^2_{red} (dof)	$F_{3-10\text{keV}}$
10002015001	5.47 ± 0.34	0.28 ± 0.03	<2.70 × 10 ⁻³	1.09 (731)	1.05 ± 0.01
10002016001	7.64 ± 0.57	0.41 ± 0.05	(1.25 ± 0.51) × 10 ⁻²	1.21 (656)	1.16 ± 0.01
60002023006	8.27 ± 0.79	0.40 ± 0.08	(9.11 ± 4.32) × 10 ⁻³	0.95 (556)	0.77 ± 0.01
60002023010	10.17 ± 1.43	0.52 ± 0.10	(4.51 ± 3.20) × 10 ⁻²	1.01 (565)	0.99 ± 0.01
60002023012	6.65 ± 0.90	0.42 ± 0.08	(4.94 ± 1.34) × 10 ⁻²	1.01 (582)	1.13 ± 0.01
60002023014	6.97 ± 1.50	0.34 ± 0.08	<4.70 × 10 ⁻³	1.05 (414)	0.44 ± 0.01
60002023016	6.71 ± 0.85	0.32 ± 0.06	<2.90 × 10 ⁻³	1.04 (552)	1.14 ± 0.01
60002023018	7.20 ± 1.03	0.33 ± 0.06	<2.50 × 10 ⁻³	0.96 (503)	0.87 ± 0.07
60002023020	8.22 ± 1.25	0.52 ± 0.10	(7.65 ± 3.01) × 10 ⁻²	0.99 (587)	1.16 ± 0.01
60002023022	8.06 ± 0.31	0.51 ± 0.03	(8.77 ± 1.10) × 10 ⁻²	1.04 (890)	2.82 ± 0.01
60002023024	12.73 ± 1.41	0.63 ± 0.04	(8.03 ± 3.02) × 10 ⁻²	1.02 (614)	4.25 ± 0.03
60002023025	11.31 ± 0.39	0.70 ± 0.01	0.36 ± 0.01	1.04 (1420)	6.62 ± 0.01
60002023026	22.10 ± 3.05	1.01 ± 0.13	0.77 ± 0.15	1.01 (395)	11.72 ± 0.12
60002023027	23.38 ± 3.51	1.04 ± 0.16	0.82 ± 0.03	0.91 (1011)	14.05 ± 0.15
60002023029	14.67 ± 1.19	0.74 ± 0.03	0.22 ± 0.02	1.09 (908)	5.27 ± 0.01
60002023031	25.10 ± 1.75	1.33 ± 0.03	2.50 ± 0.04	1.06 (1422)	14.90 ± 0.18
60002023033	10.50 ± 0.77	0.71 ± 0.03	0.50 ± 0.03	0.95 (1010)	5.55 ± 0.01
60002023035	13.17 ± 1.02	0.94 ± 0.05	1.54 ± 0.05	1.03 (1171)	5.95 ± 0.02
60002023037	12.64 ± 0.98	0.66 ± 0.11	(8.80 ± 3.50) × 10 ⁻²	1.01 (564)	0.96 ± 0.01
60002023039	5.91 ± 0.47	0.30 ± 0.10	<3.01 × 10 ⁻³	0.90 (515)	0.90 ± 0.01
60202048002†	7.35 ± 0.58	0.48 ± 0.04	0.13 ± 0.04	0.98 (999)	2.89 ± 0.02
60202048004†	12.52 ± 1.49	0.75 ± 0.08	0.37 ± 0.05	0.95 (987)	3.04 ± 0.01
60202048006†	11.67 ± 1.13	0.67 ± 0.05	0.25 ± 0.04	1.05 (986)	3.06 ± 0.01
60202048008†	8.43 ± 0.59	0.37 ± 0.04	(1.95 ± 0.97) × 10 ⁻²	0.95 (704)	0.91 ± 0.02

Note: Observation details are given in Paper-I, except for the pointings marked by † symbol which are given in Table 1. ϵ_p , in units of keV and $F_{3-10\text{keV}}$, in units of 10⁻¹⁰ erg cm⁻² s⁻¹ are calculated from the best-fit EDD model.

3.1 Turbulence index and κ

The escape of the electron from the vicinity of the shock is related to the spatial diffusion. In the jet medium, the scattering of the particle by the magnetohydrodynamic wave associated with the turbulence governs the spatial diffusion (Blandford & Eichler 1987). We express the turbulent energy spectrum $W(k)$ as,

$$W(k) \propto k^{-q} \quad (25)$$

where, k is the wave number and the range of the turbulent spectral index is $1 \leq q \leq 2$. The lower limit, $q = 1$, corresponds to Bohm diffusion where the mean free path scales as the gyroradius of the charged particle. On the other hand, the upper limit, $q = 2$, corresponds to the hard-sphere diffusion approximation where the mean free path is independent of the energy of the charged particle. The diffusion due to Kolmogorov type turbulence corresponds to $q = 5/3$, and in case of Kraichnan type $q = 3/2$ (Teraki & Asano 2019).

The escape time-scale from the acceleration region due to this spatial diffusion can be written as (Schlickeiser 2002),

$$t_{esc} \propto E^{q-2} \quad (26)$$

Comparing with equation (2) we find the parameter κ as, $\kappa = 2 - q$ and the allowed range of κ will be $0 < \kappa < 1$. For Kolmogorov type of turbulence, $\kappa = 1/3$ and in case of Kraichnan type, $\kappa = 1/2$. From Figure 1, it is evident that the best-fit κ largely satisfies within the allowed range. Most of the fitted κ values are consistent with Kolmogorov and Kraichnan case with some falling in between the Kraichnan and Bohm limit. Incidentally, no observations favoured the hard-sphere limit in the underlying assumptions of EDD model. In addition, two points fall beyond the Bohm limit are unphysical and highlight the limitation of EDD model. We further identify the probable association of the flux level with the type of turbulence by performing the correlation analysis between the integrated flux (F) and κ . In Figure 1 (top), we plot the $\ln F$ against the best-fit κ for the observations considered in the present work. A strong positive correlation between $\ln F$ and κ is witnessed with $r = 0.91$; $P_p = 6.35 \times 10^{-10}$ and $\rho = 0.85$; $P_s = 1.36 \times 10^{-7}$ when the spectral fitting is performed on *NuSTAR* observation alone. However, the correlation reduced for the case of simultaneous XRT – *NuSTAR* spectral fit, and this again hints the EDD model may not be favourable at low energies. From the positive correlation between $\ln F$ and κ , one can speculate that the magnetohydrodynamic turbulence in the jet of Mkn 421 tend to approach the Bohm limit during high flux.

4 CHARACTERISTICS OF FIT PARAMETERS

The strong linear correlation between $\ln \psi$ and κ , put together with equation (13), indicates the quantity $\delta B E_0^2$ is nearly constant for Mkn 421, independent of observed flux states. This quantity can be estimated from the slope of the linear fit to $\ln \psi$ vs κ plot. For the case of *NuSTAR* observation, a least-square fit to these quantities, taking into account the uncertainties (Press et al. 1992), resulted in slope $a = 1.44 \pm 0.08$ and the y-intercept $b = 1.41 \pm 0.05$ with betherness of fit q -value = 0.26. Likewise, the least square fit for the case of simultaneous XRT-*NuSTAR* analysis, resulted in

slope $a = 1.96 \pm 0.18$ and the y-intercept $b = 1.05 \pm 0.14$ with betherness of fit q -value = 0.22.

The slope of the best-fit line can be used to estimate the product δB , provided if E_0 can be eliminated. From equation (13), the slope of the linear relation between $\ln \psi$ and κ will be,

$$a \approx \frac{1}{2} \ln \left[10^{19} \left(\frac{1+z}{\delta B} \right) \left(\frac{E_0}{\text{keV}} \right)^{-2} \right] \quad (27)$$

and the y-intercept

$$b = \ln \xi_0 \quad (28)$$

Since in ϵF_ϵ representation the spectral slope at ϵ_p is zero, from equation (17) and (28) we obtain,

$$E_0 = E_p \exp \left(\frac{b}{\kappa} \right) \quad (29)$$

where, E_p is the electron energy responsible for the emission at ϵ_p . Under synchrotron theory, E_p and ϵ_p are related as (Rybicki & Lightman 1985; Shu 1991)

$$\epsilon_p \approx \left(\frac{\delta}{1+z} \right) \left(\frac{E_p}{mc^2} \right)^2 \left(\frac{eB}{2\pi mc} \right) \quad (30)$$

If ϵ_{ic} is the energy at which the γ -ray component of the SED peaks then assuming a synchrotron self Compton origin we can express (Rybicki & Lightman 1985)

$$\epsilon_{ic} \approx \left(\frac{\delta}{1+z} \right) \left(\frac{E_p}{mc^2} \right)^4 \left(\frac{eB}{2\pi mc} \right) \quad (31)$$

From equations (30) and (31)

$$E_p = mc^2 \sqrt{\frac{\epsilon_{ic}}{\epsilon_p}} \quad (32)$$

Finally, using equations (27), (29) and (32), we obtain the product of δB in terms of the best-fit values of the linear relation between $\ln \psi$ and κ as,

$$(\delta B)_{\text{EDD}} \approx 3.75 \times 10^{10} (1+z) \left(\frac{\epsilon_p}{\text{keV}} \right) \left(\frac{\epsilon_{ic}}{\text{MeV}} \right)^{-1} \exp \left[-2 \left(a + \frac{b}{\kappa} \right) \right] \quad (33)$$

Note that the above equation highlights the association of the energy dependence of the particle escape time-scale with the source magnetic field and the Doppler factor of the emission region.

An alternate expression of δB can be obtained in terms of the SED peak energies using equations (30), (31) and (32) as,

$$(\delta B)_{\text{peak}} \approx 8.6 \times 10^7 (1+z) \left(\frac{\epsilon_p}{\text{keV}} \right)^2 \left(\frac{\epsilon_{ic}}{\text{MeV}} \right)^{-1} \quad (34)$$

If the energy dependence of the escape time-scale is related to the product of the source magnetic field and the Doppler factor then one would expect the δB estimates using equations (33) and (34) to be equal. However, to verify this, prior knowledge of the SED peak energies is required. For ϵ_p , besides using the values obtained from EDD model, we also fit the simultaneous XRT – *NuSTAR* observations using *eplogpar* model as an alternate estimate as discussed in §3. The synchrotron peak values corresponding to the latter are denoted as $\epsilon_{p,lp}$ and given in Table 3. The non-availability of simultaneous γ -ray observations do not allow us to identify ϵ_{ic} and hence, we employ an indirect method to estimate ϵ_{ic} from the archival peak energies.

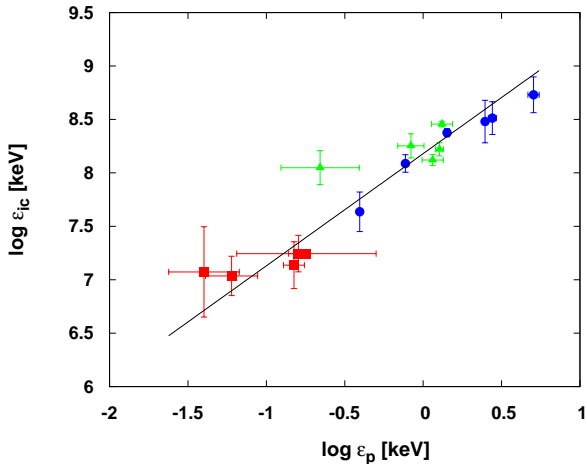


Figure 3. The correlation plot between the quasi-simultaneous archival ϵ_p and ϵ_{ic} . The red boxes are for MJD 56307 – 56362, where the ϵ_p values were estimated using *eplogpar* fit of XRT data and corresponding ϵ_{ic} were extracted using the spectral information given in Baloković et al. (2016). The blue circles were extracted using the spectral information given in Bartoli et al. (2016) for MJD 55144 – 56106. The green triangles are for MJD 55240 – 55246 where the ϵ_p values were estimated using *eplogpar* fit of XRT data and the corresponding ϵ_{ic} extracted from Kapanadze et al. (2016). The black line represents the best-fit straight line.

4.1 Compton Spectral Peak (ϵ_{ic})

For an appropriate estimate of ϵ_{ic} , we study the correlation between the archival SED peaks (ϵ_p and ϵ_{ic}) extracted from simultaneous/near-simultaneous multi wavelength observations during different flux states (Baloković et al. 2016; Bartoli et al. 2016; Kapanadze et al. 2016). The ϵ_p during the period MJD 55144-56106 is directly obtained from Bartoli et al. (2016); whereas for MJD 56307-56362, we fitted the XRT observations using *eplogpar* model to estimate ϵ_p . The ϵ_{ic} during both these periods are estimated by extrapolating the power-law γ -ray spectra corresponding to *Fermi* and MAGIC/VERITAS/ARGO-YBJ observations (Bartoli et al. 2016; Baloković et al. 2016). In Figure 3, these estimates are represented as blue solid circles for MJD 55144-56106 and red solid squares for MJD 56307-56362. For the period MJD 56393-56397, we estimate ϵ_p from log-parabola spectral analysis of simultaneous XRT–*NuSTAR* observations and the corresponding ϵ_{ic} values are obtained from the estimation using log-parabola spectral fit of MAGIC observations, performed by Kapanadze et al. (2016) and Preziuso (2013). These estimates are shown as green solid triangles in Figure 3.

A Spearman rank correlation analysis between this archival ϵ_p and ϵ_{ic} show a strong positive correlation with $\rho = 0.89$ and $P_s = 3.85 \times 10^{-6}$. Additionally, the Pearson analysis supported a linear correlation with $r = 0.91$ and $P_p = 1.76 \times 10^{-6}$ and consequently, we perform a linear regression analysis between ϵ_p and ϵ_{ic} . A least-square fit between these quantities gave us the relation,

$$\log \epsilon_{ic} = (0.90 \pm 0.08) \log \epsilon_p + (8.16 \pm 0.05) \quad (35)$$

with q -value = 0.21. We used equation (35) to infer ϵ_{ic} corresponding to the synchrotron peak estimated from simultaneous XRT–*NuSTAR* observations used in this work. The inferred values of ϵ_{ic} are given in column 7 and 9 of Table 3. It should be noted that the best-fit line obtained using a least-square fit shown in Figure 3 involves data points with $\epsilon_p < 0.5$ keV, which is beyond the observational energy range of XRT. However, even considering only the data point with $\epsilon_p \geq 0.5$ keV the least-square fit only shows a marginal change with best-fit values, slope = 0.92 ± 0.15 and the y -intercept = 8.21 ± 0.03 .

The knowledge of ϵ_p and ϵ_{ic} allow us to evaluate δB described by equations (33) and (34) and these estimates are given in Table 4. In figure 4, we plot these δB values along with the identity line. The δB values are reasonably close to the identity lines particularly when ϵ_p is estimated using *eplogpar* model. This may again be associated with the weakness of the EDD model to explain the soft X-ray spectrum. We also note a large variation in δB and this may probably reflect the extreme variability behaviour of the source. Absence of a definite consensus on the range of these parameters may support this argument (Dondi & Ghisellini 1995; Fossati et al. 2008; Mankuzhiyil et al. 2011; Bartoli et al. 2016; Kapanadze et al. 2016; Baloković et al. 2016; Banerjee et al. 2019). Alternatively, this variation in δB may be associated with the inaccurate estimation of the spectral peak energies or the combination of both. Nevertheless, this result open up the avenue where the microscopic description about the emitting electron distribution is related to the parameters governing the overall SED of the source.

5 DISCUSSION AND SUMMARY

The X-ray spectral curvature of Mkn 421 is interpreted as the result of energy-dependent electron diffusion from the acceleration region (EDD model). Unlike the log-parabola model, the EDD model parameters, ψ and κ show strong correlation. In this work, we perform a careful investigation of the EDD model and the observed correlations. We identify the photon energy at which the synchrotron spectral component peaks can correlate/anti-correlate with the spectral curvature at this energy. The sense of the correlation is determined by the parameter ψ , when $\psi > 1$, the correlation is positive and in case of $\psi < 1$ the quantities are anti correlated. The spectral fitting of Mkn 421 for the observations during the period MJD 56115-56401 and 57756-57839 indicate $\psi > 1$ and this suggests the correlation to be positive. This is further verified by performing correlation analysis between the parameters κ and ϵ_p using the EDD model with ϵ_p as a fit parameter.

Addition of soft X-ray information from XRT marginally reduces the correlation between the fit parameters and also shows relatively poor fits to some of the combined XRT – *NuSTAR* spectra, suggesting the EDD model to be better agreeable at hard X-rays. A possible reason can be, the effect of escape time-scale is more prominent at higher electron energies. Another reason may be related to the simplicity of the model and the underlying

Table 3. The best-fit EDD model parameters and the estimated quantities for the simultaneous XRT – NuSTAR observations.

Obs. ID		EDD model				ϵ_{ic}	$\epsilon_{p,lp}$	$\epsilon_{ic,lp}$	$F_{0.3-10\text{keV}}$
XRT	NuSTAR	ψ	κ	ϵ_p (keV)	χ_{red}^2 (dof)	(GeV)	(keV)	(GeV)	
[1]	[2]	[3]	[4]	[5]	[6]	[7]	[8]	[9]	[10]
00080050006	60002023014	7.96 ± 1.50	0.39 ± 0.08	$(4.49 \pm 1.50) \times 10^{-3}$	1.20 (779)	1.11 ± 0.33	0.06 ± 0.01	11.49 ± 1.72	3.41 ± 0.03
00080050007	60002023016	9.65 ± 0.85	0.48 ± 0.06	$(1.13 \pm 0.66) \times 10^{-2}$	1.05 (760)	2.55 ± 1.34	0.15 ± 0.04	26.21 ± 6.29	7.37 ± 0.17
00080050011	60002023018	12.28 ± 1.03	0.55 ± 0.06	$(1.66 \pm 0.22) \times 10^{-2}$	1.008(921)	3.61 ± 0.43	0.16 ± 0.01	27.77 ± 1.56	5.88 ± 0.03
00032792001†	60002023025†	6.03 ± 0.65	0.42 ± 0.01	$(3.54 \pm 0.40) \times 10^{-2}$	1.48 (1836)	7.14 ± 0.72	0.18 ± 0.01	30.88 ± 1.54	11.83 ± 0.08
00080050016	60002023025	7.61 ± 0.28	0.53 ± 0.01	$(7.41 \pm 0.79) \times 10^{-2}$	1.29 (1780)	14.02 ± 1.19	0.38 ± 0.02	60.50 ± 2.86	17.88 ± 0.19
00080050019	60002023026	47.10 ± 12.35	1.36 ± 0.09	0.55 ± 0.02	1.20 (903)	84.39 ± 3.03	1.27 ± 0.04	179.23 ± 5.08	42.02 ± 1.04
00080050019	60002023027	39.24 ± 4.05	1.28 ± 0.04	0.49 ± 0.02	1.28 (1519)	76.06 ± 2.79	1.33 ± 0.03	186.83 ± 3.79	41.86 ± 0.27
00032792002†	60002023029†	20.75 ± 0.99	0.90 ± 0.02	0.18 ± 0.01	1.27 (1449)	31.96 ± 0.95	0.64 ± 0.01	96.73 ± 1.36	15.95 ± 0.07
00035014062	60002023033	10.50 ± 0.77	0.72 ± 0.03	0.20 ± 0.02	0.98 (1309)	33.95 ± 3.05	0.84 ± 0.07	123.55 ± 9.26	16.85 ± 0.23
00035014065	60002023035	13.17 ± 1.02	0.92 ± 0.05	0.63 ± 0.01	1.29 (1733)	95.36 ± 2.45	1.51 ± 0.03	209.44 ± 3.74	17.93 ± 0.12
00035014066	60002023037	12.64 ± 0.98	0.66 ± 0.11	$(1.92 \pm 0.11) \times 10^{-2}$	1.10 (996)	4.12 ± 0.21	0.11 ± 0.01	19.82 ± 1.62	5.83 ± 0.31
00035014067	60002023039	5.91 ± 0.47	0.44 ± 0.10	$(1.06 \pm 0.12) \times 10^{-2}$	1.05 (931)	2.41 ± 0.24	0.12 ± 0.01	21.44 ± 1.60	6.40 ± 0.64
00034228166†	60202048008†	5.41 ± 0.38	0.35 ± 0.07	$(3.67 \pm 1.10) \times 10^{-3}$	1.02 (879)	0.92 ± 0.25	0.07 ± 0.06	12.87 ± 1.03	3.82 ± 0.09
00034228146†	60202048006†	8.85 ± 1.36	0.68 ± 0.06	0.26 ± 0.04	1.04 (1012)	43.05 ± 6.10	1.47 ± 0.12	204.44 ± 15.02	8.75 ± 0.15
00034228110†	60202048002†	9.90 ± 0.59	0.77 ± 0.02	0.39 ± 0.01	1.16 (1483)	61.93 ± 2.57	1.30 ± 0.20	183.04 ± 25.34	8.79 ± 0.21
00081926001†	60202048004†	11.17 ± 1.12	0.83 ± 0.04	0.43 ± 0.03	1.005 (1266)	67.62 ± 5.37	1.61 ± 0.47	221.89 ± 58.29	8.96 ± 0.13

Note: Columns:- [3],[4]&[5]: best-fit EDD model parameters; [7]: Compton peaks estimated from ϵ_p using equation (35); [8]&[9]: synchrotron peaks estimated using *eplogpar* model fit and the corresponding Compton peaks estimated from $\epsilon_{p,lp}$ using equation (35); [10]: 0.3 –10 keV integrated flux in units of 10^{-10} erg cm^{-2} s^{-1} , calculated from the best-fit EDD model. Observation details of XRT are given in Paper-I, except for the pointings marked by † symbol which are given in Table 1.

assumptions. A detailed description of the model including stochastic acceleration (Fermi second-order process) and/or shock-drift acceleration may have the capability to explain the spectral behaviour over a broad energy range. For instance, (Katarzyński et al. 2006) have studied the evolution of the particle spectrum considering the combination of shock and stochastic acceleration mechanisms. Similarly, Böttcher & Baring (2019) have illustrated the radiative signatures by considering time-dependent evolution of particles due to a combination of diffusive shock acceleration and shock drift acceleration. We have assumed a monoenergetic injection of particles into the shock which is then accelerated to relativistic energies; however, a detailed description may involve an energy-dependent particle injection (Summerlin & Baring 2012; Baring et al. 2017). Nevertheless, an exact description may increase the number of free parameters and constraining them using statistical fitting procedure over a narrow energy band may be impossible or misleading.

The energy dependence of the escape time-scale of the EDD model can be associated with the magnetohydrodynamic turbulence responsible for spatial diffusion of the particle. For the case of Mkn 421, we found this energy dependence satisfies well within the constraints imposed by the hard-sphere and Bohm diffusion limits. The observed strong correlation between the integrated flux and the energy index of the escape time-scale signifies the high flux states may be associated with the turbulence shifting from Kolmogorov/Kraichnan type to Bohm limit. Incidentally, the spectral fitting of the curved X-ray spectrum by EDD model do not favour hard-sphere type turbulence. Under hard-sphere approximation, the parameter κ will be zero

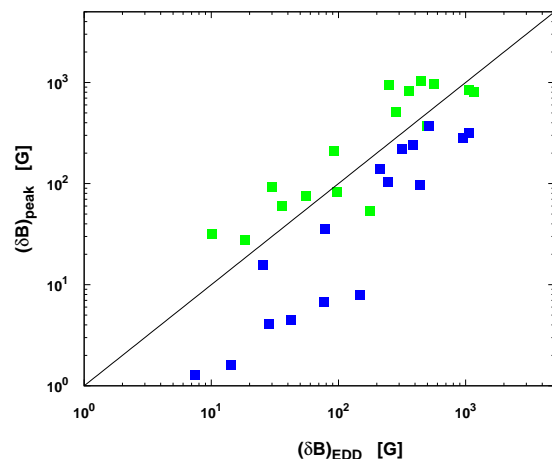


Figure 4. The plot between $(\delta B)_{EDD}$ and $(\delta B)_{peaks}$ obtained using equations (33) and (34) for the simultaneous XRT–NuSTAR data. The blue boxes represent (δB) estimation where ϵ_p values were determined from the EDD model fit. On the other hand, the green boxes indicate these estimations where $\epsilon_{p,lp}$ values were estimated using *eplogpar* fit (Table 4). The black line represents the identity line.

(equation 26) and from equation (4) it is evident EDD model predicts a power-law electron distribution. Since the X-ray spectra of Mkn 421 is significantly curved, the EDD model does not favour hard-sphere type turbulence. However, this conclusion should be dealt with caution due

Table 4. Estimations of δB from equations (33) and (34) using simultaneous XRT–*NuSTAR* observations.

XRT Obs. ID	<i>NuSTAR</i> Obs. ID	$(\delta B)_{\text{EDD}}$	$(\delta B)_{\text{peak}}$	$(\delta B)_{\text{EDD,lp}}$	$(\delta B)_{\text{peak,lp}}$
[1]	[2]	[3]	[4]	[5]	[6]
00080050006	60002023014	14.17	1.60	18.37	27.77
00080050007	60002023016	42.67	4.42	55.26	76.11
00080050011	60002023018	77.38	6.75	97.06	81.71
00032792001	60002023025	25.60	15.54	30.12	93.01
00080050016	60002023025	77.89	35.45	91.63	211.60
00080050019	60002023026	1067.30	317.80	1160.47	797.88
00080050019	60002023027	957.98	279.88	1058.58	839.44
00032792002	60002023029	435.19	97.05	492.17	375.45
00035014062	60002023033	244.49	104.44	282.22	506.36
00035014065	60002023035	516.96	369.08	564.19	965.23
00035014066	60002023037	148.36	7.93	176.66	54.11
00035014067	60002023039	28.48	4.12	36.30	59.54
00034228166	60202048008	7.50	1.28	10.05	31.93
00034228146	60202048006	211.42	139.38	251.41	937.14
00034228110	60202048002	315.88	217.73	356.29	818.64
00081926001	60202048004	388.49	242.42	443.32	1035.77

Note: δB is in the units of Gauss. Columns [3]&[4]: (δB) estimates involve ϵ_{ic} values evaluated from the best-fit ϵ_p values using EDD model. [5]&[6]: (δB) estimates involve ϵ_{ic} values evaluated from best-fit $\epsilon_{p,lp}$ values using *eplogpar* model.

to varying underlying assumptions of the EDD model. Presence of two data points beyond Bohm limit (Figure 1 & 2) further indicate the limitation of EDD model. It should also be noted that studies on X-ray spectra of Mkn 421 using stochastic acceleration scenario have supported hard-sphere type turbulence (Tramacere et al. 2011; Asano & Hayashida 2018). By means of a Monte Carlo description, Tramacere et al. (2011) have demonstrated the transition from Kraichnan turbulence into the hard-sphere type. Similar results are also reported by several authors for Mkn 421 for different observational epochs (Kapanadze et al. 2018a,b, 2020).

A least square fit to the EDD model parameters allow us to derive an expression for the product of the source magnetic field and the jet Doppler factor, in terms of synchrotron and the Compton spectral peaks. The peak energy of the synchrotron component is obtained by fitting the simultaneous XRT–*NuSTAR* observations by EDD and *eplogpar* models; whereas, for the peak energy of the Compton spectral component an indirect approach involving archival observations is employed. The product of the source magnetic field and the jet Doppler factor estimated through this approach matches reasonably well with the estimates attained through synchrotron and synchrotron self Compton theory. This possibly highlights the link between the shape of electron distribution with the parameters deciding the broadband spectrum of the source. The estimated product of the source magnetic field and the jet Doppler factor varies

over a wide range $\sim 7 - 1160$. This may either reflect the extreme variable behaviour of the source or may be associated with the inaccurate estimation of peak photon energies.

The EDD model can be further refined to represent a more realistic scenario by incorporating the exact form of the momentum diffusion and/or an appropriate energy dependence of the acceleration time scale. Future works, the inclusion of other available observational signatures will allow us to relax various assumptions and let us step towards a global picture of particle acceleration and diffusion in blazar jets. Such changes also have the potential to refine/reject the scenario portrayed by the EDD model.

Acknowledgements

The authors thank the anonymous referee for useful suggestions and comments. This research has made use of data, software, and/or web tools obtained from NASA's High Energy Astrophysics Science Archive Research Center (HEASARC), a service of the Goddard Space Flight Center and the Smithsonian Astrophysical Observatory. RG and PG would like to thank the ISRO, Department of Space, India for the grant under "Space Science Promotion". PG would like to thank IUCAA, BARC and HBCSE for their hospitality during the visit. RG thanks the IUCAA associateship programme.

DATA AVAILABILITY

The data underlying this article are available in the HEASARC archive at <https://heasarc.gsfc.nasa.gov/>.

REFERENCES

- Abdo A. A., et al., 2011, *ApJ*, **736**, 131
- Acciari V. A., et al., 2011, *ApJ*, **738**, 25
- Aleksić J., et al., 2015a, *A&A*, **576**, A126
- Aleksić J., et al., 2015b, *A&A*, **578**, A22
- Arnaud K. A., 1996, in Jacoby G. H., Barnes J., eds, *Astronomical Society of the Pacific Conference Series Vol. 101, Astronomical Data Analysis Software and Systems V*. p. 17
- Asano K., Hayashida M., 2018, *ApJ*, **861**, 31
- Asano K., Takahara F., Kusunose M., Toma K., Kakuwa J., 2014, *ApJ*, **780**, 64
- Baloković M., et al., 2016, *ApJ*, **819**, 156
- Banerjee B., Joshi M., Majumdar P., Williamson K. E., Jorstad S. G., Marscher A. P., 2019, *MNRAS*, **487**, 845
- Baring M. G., Böttcher M., Summerlin E. J., 2017, *MNRAS*, **464**, 4875
- Bartoli B., et al., 2011, *ApJ*, **734**, 110
- Bartoli B., et al., 2016, *ApJS*, **222**, 6
- Becker P. A., Le T., Dermer C. D., 2006, *The Astrophysical Journal*, **647**, 539
- Begelman M. C., Blandford R. D., Rees M. J., 1984, *Reviews of Modern Physics*, **56**, 255
- Blandford R., Eichler D., 1987, *Phys. Rep.*, **154**, 1
- Błażejowski M., et al., 2005, *ApJ*, **630**, 130
- Böttcher M., Baring M. G., 2019, *ApJ*, **887**, 133
- Böttcher M., Dermer C. D., 2010, *ApJ*, **711**, 445
- Dondi L., Ghisellini G., 1995, *MNRAS*, **273**, 583
- Donnarumma I., et al., 2009, *ApJ*, **691**, L13
- Finke J. D., Dermer C. D., Böttcher M., 2008, *ApJ*, **686**, 181
- Fossati G., et al., 2000, *ApJ*, **541**, 166
- Fossati G., et al., 2008, *ApJ*, **677**, 906
- Giebels B., Dubus G., Khélifi B., 2007, *A&A*, **462**, 29
- Goswami P., Sahayanathan S., Sinha A., Misra R., Gogoi R., 2018, *MNRAS*, **480**, 2046
- Horan D., et al., 2009, *ApJ*, **695**, 596
- Hovatta T., et al., 2015, *MNRAS*, **448**, 3121
- Jagan S. K., Sahayanathan S., Misra R., Ravikumar C. D., Jeena K., 2018, *MNRAS*, **478**, L105
- Kakuwa J., 2016, *ApJ*, **816**, 24
- Kapanadze B., et al., 2016, *ApJ*, **831**, 102
- Kapanadze B., et al., 2018a, *ApJ*, **854**, 66
- Kapanadze B., Vercellone S., Romano P., Hughes P., Aller M., Aller H., Kharshiladze O., Tabagari L., 2018b, *ApJ*, **858**, 68
- Kapanadze B., et al., 2020, *ApJS*, **247**, 27
- Kardashev N. S., 1962, *Soviet Ast.*, **6**, 317
- Katarzyński K., Walczewska K., 2010, *A&A*, **510**, A63
- Katarzyński K., Ghisellini G., Mastichiadis A., Tavecchio F., Maraschi L., 2006, *A&A*, **453**, 47
- Kirk J. G., Rieger F. M., Mastichiadis A., 1998, *A&A*, **333**, 452
- Krawczynski H., et al., 2001, *ApJ*, **559**, 187
- Kusunose M., Takahara F., Li H., 2000, *ApJ*, **536**, 299
- Lewis T. R., Becker P. A., Finke J. D., 2016, *ApJ*, **824**, 108
- Mankuzhiyil N., Ansoldi S., Persic M., Tavecchio F., 2011, *The Astrophysical Journal*, **733**, 14
- Massaro E., Perri M., Giommi P., Nesci R., 2004, *A&A*, **413**, 489
- Massaro F., Tramacere A., Cavaliere A., Perri M., Giommi P., 2008, *A&A*, **478**, 395
- Mastichiadis A., Kirk J. G., 1997, *A&A*, **320**, 19
- McEnery J., et al., 1997, in *International Cosmic Ray Conference*. p. 257 ([arXiv:astro-ph/9706125](https://arxiv.org/abs/astro-ph/9706125))
- Melrose, D.B. 1980, *Plasma Astrophysics: V2*. (New York:Gordon and Breach)
- Padovani P., Giommi P., 1995, *ApJ*, **444**, 567
- Press W. H., Teukolsky S. A., Vetterling W. T., Flannery B. P., 1992, *Numerical recipes in FORTRAN. The art of scientific computing*
- Prezioso S., 2013, PhD thesis, Univ. Pisa
- Punch M., et al., 1992, *Nature*, **358**, 477
- Rybicki G. B., Lightman A. P., 1985, *Radiative Processes in Astrophysics*. (John Wiley & Sons)
- Sahayanathan S., Godambe S., 2012, *MNRAS*, **419**, 1660
- Schlickeiser R., 2002, *Cosmic Ray Astrophysics*. (Berlin: Springer)
- Shu F., 1991, *Physics of Astrophysics: Volume I Radiation*
- Sinha A., Shukla A., Misra R., Chitnis V. R., Rao A. R., Acharya B. S., 2015, *A&A*, **580**, A100
- Stawarz L., Petrosian V., 2008, *The Astrophysical Journal*, **681**, 1725
- Summerlin E. J., Baring M. G., 2011, *The Astrophysical Journal*, **745**, 63
- Summerlin E. J., Baring M. G., 2012, *ApJ*, **745**, 63
- Tanihata C., Kataoka J., Takahashi T., Madejski G. M., 2004, *ApJ*, **601**, 759
- Teraki Y., Asano K., 2019, *ApJ*, **877**, 71
- Tramacere A., Massaro F., Cavaliere A., 2007, *A&A*, **466**, 521
- Tramacere A., Giommi P., Perri M., Verrecchia F., Tosti G., 2009, *A&A*, **501**, 879
- Tramacere A., Massaro E., Taylor A. M., 2011, *ApJ*, **739**, 66
- Yan D., Zhang L., Yuan Q., Fan Z., Zeng H., 2013, *ApJ*, **765**, 122
- Zheng Y. G., Kang S. J., Li J., 2014, *MNRAS*, **442**, 3166

This paper has been typeset from a $\text{\TeX}/\text{\LaTeX}$ file prepared by the author.